ACS Photonics

Open Access

pubs.acs.org/journal/apchd5

Article

Characterization of the 3D-Optical Properties of van der Waals Materials with Deep Learning-Based Coherent Fourier Scatterometry

Anubhav Paul,* Kumar Rishav, Guus Klootwijk, Mitradeep Sarkar, Onima Bisht, Zizheng Li, Sonia Conesa-Boj, Georgia T. Papadakis, and Silvania F. Pereira

Cite This: ACS Photonics 2026, 13, 224−235

Read Online

ACCESS | Metrics & More | Article Recommendations | Supporting Information

ABSTRACT: The characterization of optical anisotropy in thin van der Waals (vdW) materials is crucial for both fundamental studies and nanophotonic applications. However, conventional techniques such as spectroscopic ellipsometry face significant limitations in measuring out-of-plane anisotropy and require large-area, uniform films. In this work, we present a novel framework based on coherent Fourier scatterometry (CFS) combined with deep learning for the rapid, label-free characterization of in-plane and out-of-plane refractive indices of anisotropic thin films. We designed a specialized deep neural network, AnisoVision, and trained it on simulated far-field angular spectra from multilayer stacks using the 4 × 4 Berreman matrix formalism. To efficiently capture the directional dependence of anisotropy, we utilize radially polarized light and extract only three far-field azimuthal cross sections (0, 45, 90°), enabling robust retrieval while minimizing data requirements. Our method demonstrates accurate index retrieval for both isotropic and anisotropic materials, including uniaxial h-BN and biaxial α-MoO_3 flakes of varying thickness. We further validate the model's stability by testing multiple flakes of the same material across a range of thicknesses, yielding consistent optical constants. Our approach is single-shot, nondestructive, and applicable to localized sample regions, making it suitable for heterogeneous or exfoliated samples. Additionally, the technique can be readily extended to broadband operation for spectroscopic analysis. Our work establishes CFS coupled with deep learning as a powerful platform for high-throughput optical metrology of low-dimensional materials.

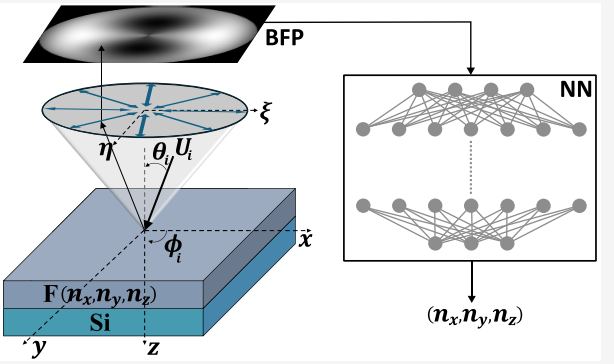

KEYWORDS: *coherent Fourier scatterometry, deep learning metrology, anisotropic thin films, van der Waals materials, optical characterization, radial polarization*

INTRODUCTION

The optical characterization of anisotropic materials, particularly ultrathin two-dimensional (2D) van der Waals materials, plays a critical role in the design and application of next-generation photonic and optoelectronic devices.[1−6] The ability to accurately measure refractive indices along different crystal axes enables precise understanding of anisotropy, anisotropy-induced resonances, and polarization-dependent behaviors, all of which are key to tuning the optical response of materials like hexagonal boron nitride (h-BN) and α-MoO_3.[7−9] However, existing methods often fall short in providing a robust, spatially localized, and inline solution that is compatible with the nanoscale dimensions and strong optical anisotropic properties of these crystals. A noninvasive, high-resolution technique capable of extracting full anisotropic refractive index information with minimal data and single-shot acquisition would significantly advance both fundamental research and industrial metrology applications.

Traditional optical metrology methods such as spectroscopic ellipsometry are widely used to extract optical constants of thin films, including anisotropic materials.[10,11] Recent developments in imaging ellipsometry have extended its capabilities to spatially resolved mapping of anisotropic vdW flakes,[1,7,12−14] and these systems are now commercially available. Imaging ellipsometry remains the most accurate quantitative approach for such a characterization. Related methods such as microellipsometry have also been demonstrated for local micron-scale flake measurements.[15−17] However, ellipsometry inherently requires multiple angles of incidence and polar-

Received: September 9, 2025
Revised: November 27, 2025
Accepted: December 3, 2025
Published: December 17, 2025

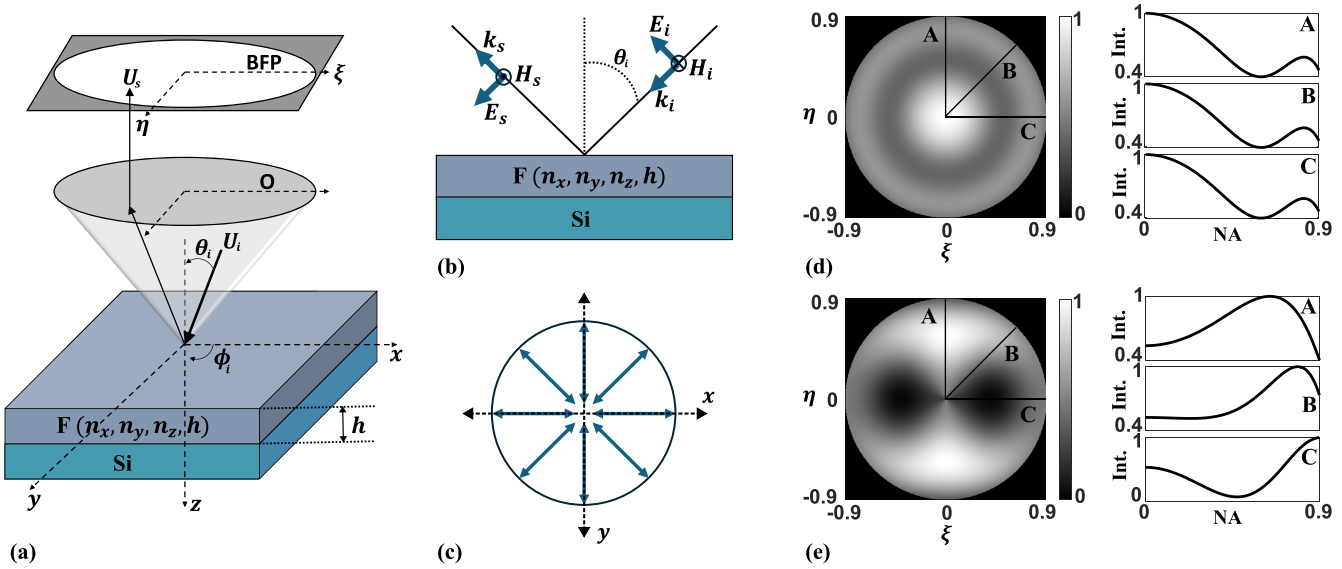

Figure 1. (a) Schematic of the CFS setup with focused field illumination and a multilayer stack comprising air, anisotropic film F(n_x, n_y, n_z, h), and silicon substrate. (b) Geometry of a single *p*-polarized plane wave interacting with the stack at an angle θ_i and azimuth ϕ_i. (c) Top-view of radial polarization showing uniform azimuthal angular coverage. (d) Simulated far-field for an isotropic film ($n_x = n_y = n_z = 1.46$). Cross sections A, B, and C correspond to azimuths ϕ = 0, 45, and 90°, respectively. (e) Simulated far-field for an anisotropic film ($n_x = 2.7$, $n_y = 1.9$, $n_z = 2.1$), showing asymmetry in angular response.

ization states and assumes macroscopic lateral uniformity. This limits its application for localized flake-based materials, such as mechanically exfoliated or transferred 2D flakes, where thickness variation, lateral inhomogeneity, and random crystal axis orientation are common, and where high optical anisotropy can only be preserved over microscopic lateral dimensions, making exfoliation essential for obtaining high-quality flakes.[18] Moreover, for out-of-plane anisotropy, ellipsometry is sensitive only in grazing-incidence configurations, which are experimentally challenging to implement for small-sized flakes.[19,20] Other methods such as scanning near-field optical microscopy (SNOM) offer subdiffraction resolution and can map local anisotropy but require complex instrumentation and suffer from limited throughput.[21−23] Quantitative phase microscopy (QPM) has also been employed for thickness and refractive index estimation of 2D materials in transmission mode, but has been limited in retrieving full anisotropic dielectric tensors.[24] These limitations highlight the need for complementary approaches that can operate in reflection with focused beams and that are robust to sample orientation.

Recent advances in coherent Fourier scatterometry (CFS) offer an attractive alternative by leveraging the angle-resolved field distribution from focused beams to infer structural and material parameters.[25−27] CFS enables single-shot, angle-resolved characterization from the back focal plane of a high-NA objective, making it particularly suitable for nanoscale patterned surfaces and flake-based layered materials. When combined with the angular spectrum decomposition of a focused beam, CFS can probe the optical response in different in-plane directions.[28,29] However, the inverse problem of retrieving optical constants from such angular data is computationally intensive, especially for anisotropic materials, where the dielectric tensor has multiple independent components.

Machine learning-based optical metrology methods have emerged as powerful tools for rapid inverse modeling, offering orders-of-magnitude speedup over traditional optimization or fitting routines.[30−32] Neural networks have been applied to retrieve thickness,[33] morphology,[34] and optical identification[35] of thin films from reflectance or scattering data. In particular, deep learning frameworks have shown promise for optical property retrieval in microscopy and scatterometry, due to their ability to generalize complex mappings from high-dimensional data.[36−38] However, most of these approaches focus on scalar (isotropic) parameters, require full-field data with a high signal-to-noise ratio, or are limited to simulation-trained models that may not generalize well to experiments.[39] Additionally, the anisotropic nature of layered crystals and their orientation dependence have not been adequately addressed in existing models.

In this work, we developed AnisoVision, a deep learning-based CFS framework tailored for the characterization of anisotropic optical properties in thin van der Waals materials. Our method combines radially polarized illumination[40] with a physically interpretable selection of angular cross sections (0, 45, and 90°) that are sufficient to distinguish between the in-plane and out-of-plane components of the dielectric tensor. By training a dedicated neural network architecture, IndexNet, on synthetic far-field profiles computed via the Berreman 4 × 4 matrix formalism, we achieve an accurate prediction of (n_x, n_y, n_z) for arbitrary flake thicknesses. The approach is robust to sample orientation, noise, and missing central data conditions often encountered in experimental CFS setups. We validate our model using experimental data from isotropic (SiN, SiO_2) and anisotropic (h-BN, α-MoO_3) flakes, demonstrating excellent agreement with the literature values and consistency across flake thicknesses. As a localized, inline, and single-shot optical method, AnisoVision provides a powerful new tool for stress measurement, material identification, and device calibration.

https://doi.org/10.1021/acsphotonics.5c02153
ACS Photonics 2026, 13, 224−235

METHODS

Concept. In this section, we introduce the angle-resolved reflection problem from multilayered anisotropic flakes and the associated theoretical framework, as implemented through the CFS platform. Figure 1(a) illustrates the overall CFS configuration, where a tightly focused laser beam is incident on a multilayer structure consisting of air, an unknown anisotropic film denoted as F(n_x, n_y, n_z, h), and a semi-infinite silicon substrate. The system is described by using a Cartesian coordinate system (x, y, z) with the z-axis normal to the surface and the origin located at the center of the illumination spot. According to the angular spectrum decomposition formalism, the tightly focused beam is decomposed into a continuous distribution of plane waves $\mathbf{U}_i(\theta_i, \phi_i)$, each characterized by a polar angle θ_i and an azimuthal angle ϕ_i, as shown in the conical illumination geometry. The angular range is determined by the numerical aperture (NA) of the objective lens (O). Upon interaction with the sample, each plane wave is partially reflected and transmitted, resulting in a net reflected field $\mathbf{U}_s(\theta_i, \phi_i)$. These fields are collected by the same objective and propagated to the back focal plane (BFP), where the angular distribution of the reflected light is recorded (coordinates (ξ, η)). This mapping between incident angles and spatial frequency at the BFP is governed by Fourier optics and is limited by the NA of the collection system.[41]

To model the interaction of each plane wave with the stack (air, F, Si), we employ the 4 × 4 matrix formalism derived from Maxwell's equations.[42] This approach enables accurate modeling of stratified media with an arbitrary anisotropy. The local geometry is shown in Figure 1(b), where an individual p-polarized plane wave (i.e., with the electric field vector $\boldsymbol{E}_i$ lying in the plane of incidence) impinges on the multilayer structure. The film layer is characterized by a dielectric tensor $\overline{\varepsilon}$ with principal components ε_x, ε_y, and ε_z, which correspond to the square of the refractive indices ($\varepsilon_i = n_i^2$ for $i = x, y$, and z). We assume that the materials are linear, nonmagnetic ($\mu = \mu_0$), and homogeneous in each layer.

Each plane wave can be treated independently, and its interaction with the stack is modeled by solving Maxwell's equations in matrix form. The state of the electromagnetic field in the z-direction is represented by a four-component field vector: $\Psi(z) = [E_x(z), H_y(z), E_y(z), -H_x(z)]^T$, which satisfies the differential equation

$$\frac{\partial}{\partial z}\Psi(z) = i\frac{\omega}{c}\Delta(z)\Psi(z) \tag{1}$$

where the 4 × 4 system matrix $\Delta(z)$ is constructed from the material tensors and the transverse wavevector $K_x = n_{\text{inc}} \sin\theta_i$. Assuming propagation in the x–z plane ($K_y = 0$), the matrix Δ takes the form[43]

$$\Delta = \begin{bmatrix} -\frac{K_x\varepsilon_{zx}}{\varepsilon_{zz}} & 1 - \frac{K_x^2}{\varepsilon_{zz}} & -\frac{K_x\varepsilon_{zy}}{\varepsilon_{zz}} & \frac{K_x}{\varepsilon_{zz}} \\ \varepsilon_{xx} - \frac{\varepsilon_{xz}\varepsilon_{zx}}{\varepsilon_{zz}} & -\frac{K_x\varepsilon_{xz}}{\varepsilon_{zz}} & \varepsilon_{xy} - \frac{\varepsilon_{xz}\varepsilon_{zy}}{\varepsilon_{zz}} & \frac{\varepsilon_{xz}}{\varepsilon_{zz}} \\ 0 & 0 & 0 & 1 \\ \varepsilon_{yx} - \frac{\varepsilon_{yz}\varepsilon_{zx}}{\varepsilon_{zz}} & -\frac{K_x\varepsilon_{yz}}{\varepsilon_{zz}} & \varepsilon_{yy} - \frac{K_x^2 + \varepsilon_{yz}\varepsilon_{zy}}{\varepsilon_{zz}} & \frac{\varepsilon_{yz}}{\varepsilon_{zz}} \end{bmatrix} \tag{2}$$

In the case of an isotropic, uniaxial, or biaxial material aligned with the coordinate axes, the off-diagonal components vanish, simplifying the matrix. The eigenmodes of the system, corresponding to forward and backward propagating (or evanescent) solutions, are obtained by diagonalizing Δ. The field evolution through each layer of thickness h is then expressed using

$$\Psi(z + h) = R(h)\Psi(z),\ R = P\exp(ik_0hQ)P^{-1} \tag{3}$$

where P contains the eigenvectors and Q is a diagonal matrix of eigenvalues (the z-components of the wavevectors). This formalism is implemented via the scattering matrix method as in the `ReticoloFilmStack` package to determine the reflected far-field pattern,[44] which ensures stability even for highly anisotropic or thick layers.

A critical aspect of our approach is the use of radially polarized illumination (Figure 1(c)), which provides a cylindrically symmetric purely p-polarized angular spectrum. For such illumination, the field satisfies $E_y = H_x = 0$, reducing the field vector to $\Psi(z) = [E_x(z), H_y(z), 0, 0]^T$. In this configuration, the optical response is independent of ε_y when the plane of incidence is aligned along the x-axis (i.e., $\phi = 0°$), making the response sensitive only to ε_x, ε_z, and h. Similarly, when the plane is along the y-axis ($\phi = 90°$), the response depends on the ε_y, ε_z, and h. For intermediate orientations such as $\phi = 45°$, all three components ε_x, ε_y, and ε_z contribute. Figure 1(d,e) demonstrates this angular dependence using simulated far-fields for two representative cases. In Figure 1(d), the film is isotropic ($n_x = n_y = n_z = 1.46$, $h = 600$ nm), producing a radially symmetric far-field pattern. In contrast, Figure 1(e) shows the far-field for an anisotropic film with $n_x = 2.7$, $n_y = 1.9$, $n_z = 2.1$, and $h = 600$ nm. The asymmetry is evident, particularly in the angular slices labeled A–C, which correspond to $\phi = 0$, 45, and 90°, respectively. The azimuthal variation encodes the anisotropy of the film. This property allows us to drastically reduce the dimensionality of both simulation and experiment. Instead of analyzing the full 2D far-field, we extract only three azimuthal cross sections (at 0, 45, and 90°), which are sufficient to uniquely retrieve n_x, n_y, and n_z for a known h. Because the radially polarized illumination always contains all azimuths (Figure 1(c)), these slices are inherently present in every measurement, eliminating the need for sample alignment or scanning.

In summary, we utilized the 4 × 4 matrix formalism to rigorously model the reflectance of each angular plane wave in the focused beam. The combination of radially polarized illumination and selective azimuthal sampling enables efficient and robust reconstruction of anisotropic optical properties, using a minimal subset of far-field data. This approach is broadly applicable to layered anisotropic materials, including but not limited to van der Waals materials.

Experimental Setup. The experimental configuration used for CFS is illustrated schematically in Figure 2. A linearly polarized He–Ne laser operating at a wavelength of $\lambda = 633$ nm serves as the illumination source. The laser beam is first coupled into a single-mode optical fiber using Lens 1 to ensure a clean Gaussian mode profile. Light emerging from the fiber is collimated using Lens 2 to produce a spatially uniform, coherent, and collimated beam. To generate spatially varying polarization states, we employ a combination of a linear polarizer and a liquid crystal polymer (LCP) vortex half-wave retarder of topological charge $m = 1$. By aligning the fast axis of the vortex retarder either parallel or perpendicular to the input

https://doi.org/10.1021/acsphotonics.5c02153
ACS Photonics 2026, 13, 224–235

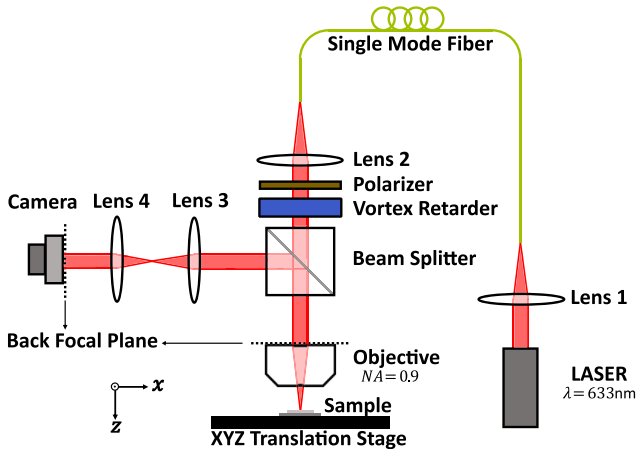

Figure 2. Schematic of the experimental setup of the CFS.

linear polarization, one can produce radially or azimuthally polarized beams, respectively. In this work, we exclusively use the radially polarized configuration, which ensures that all incident plane waves in the focused beam are *p*-polarized with respect to their local planes of incidence. The collimated, radially polarized beam is directed toward a nonpolarizing beam splitter, which transmits the beam to a high numerical aperture (NA = 0.9) microscope objective, with the beam diameter being significantly larger than the objective aperture, ensuring uniform, flat-field illumination across the entrance pupil (the calibration of the microscope objective is provided in Section 1 of the Supporting Information). This objective focuses the beam onto the sample surface, resulting in a tightly confined focal spot (nominal FWHM ≈ 491.39 nm). The sample, composed of a multilayer stack (air, anisotropic film F(n_x, n_y, n_z, h), and silicon substrate), is mounted on a piezocontrolled XYZ translation stage, allowing for precise sample positioning. In this study, we investigate four types of samples: SiN on Si, SiO_2 on Si, hexagonal-BN (h-BN) on Si, and α-MoO_3 on Si. Details of the sample preparation process are provided in the Appendix to Sample Preparation. The back-reflected light from the sample is collected by the same microscope objective and passes back through the beam splitter. A relay telescope, composed of Lens 3 and Lens 4, projects the back focal plane (BFP) of the objective onto a CCD camera. As each incident plane wave contributes to a specific direction in the BFP, the recorded image represents the far-field reflectance distribution resulting from the entire angular spectrum present in the focused beam.

An important consideration in this setup arises from the phase singularity introduced by the vortex retarder. At the beam center, where the azimuthal phase wraps by 2π, a phase singularity forms, leading to a central null-intensity in the illumination profile.[45] This singularity is transferred to the reflected field and appears as a region of an undefined phase and suppressed intensity at the center of the far-field image. As this central region contains distorted or ambiguous information, we exclude it from all data analyses and from the retrieval algorithm. This masking step is critical for ensuring accurate reconstruction of the anisotropic optical constants.

Deep Learning Architecture. To retrieve the anisotropic refractive indices n_x, n_y, and n_z of thin films from angle-resolved reflectance data, we developed a deep learning framework termed AnisoVision, illustrated schematically in Figure 3. This framework is designed to process multiview, polarization-resolved far-field signals and output accurate predictions of material parameters from minimal data. The AnisoVision model uses a custom-built architectural module called

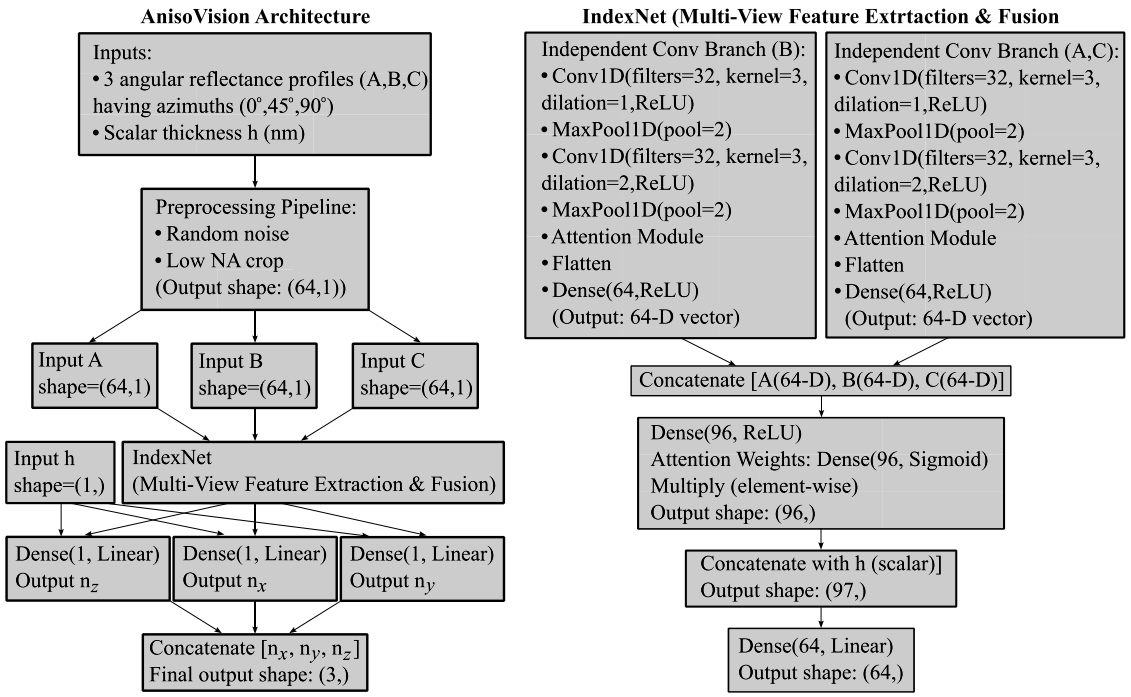

Figure 3. Schematic of the deep learning framework. The AnisoVision model accepts three far-field signals (A, B and C) and one scalar thickness value *h*. Signals A and C are processed through a shared IndexNet block comprising Conv1D, pooling, dilation, and attention layers. Signal B is processed in a similar, separate path. Extracted features are fused and passed through a global attention layer. After concatenation with *h*, the network predicts n_x, n_y, and n_z.

https://doi.org/10.1021/acsphotonics.5c02153
ACS Photonics 2026, 13, 224−235

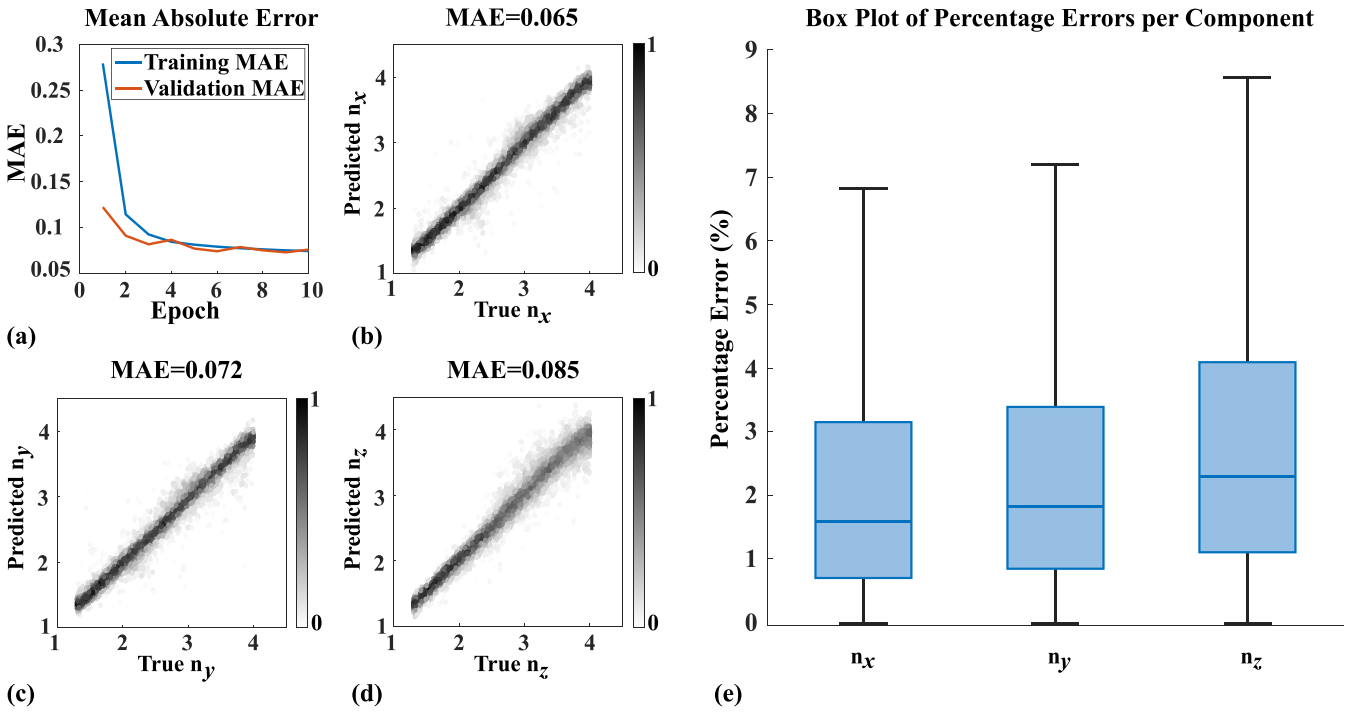

Figure 4. Performance evaluation of the AnisoVision model. (a) MAE vs epoch for training and validation sets. (b–d) Scatter density plots comparing predicted and true values for n_x, n_y, and n_z over 10,000 random test samples; corresponding MAEs are also indicated. (e) Box plot of percentage errors for each refractive index component showing the statistical spread and median error.

IndexNet, which performs joint feature extraction and fusion from multiple 1D signal channels.

The AnisoVision model accepts four inputs: three angular reflectance profiles (signals A–C), each corresponding to a fixed azimuthal slice (0, 45, and 90°), and a scalar value representing the film thickness h. The network architecture comprises a shared convolutional feature extractor, attention-based weighting modules, and a fully connected regression head.

The feature extraction pipeline for signals A and C is identical and is performed by the shared IndexNet module. This module includes a sequence of 1D convolutional layers followed by maximum pooling to extract local features and reduce dimensionality. A dilated convolutional layer is applied next to capture long-range dependences and broader contextual information. The resulting feature maps are passed through a channelwise attention mechanism that learns to amplify or suppress specific features, selectively enhancing those most relevant to the prediction task. This process yields a compact 64-dimensional representation for each input signal. Signal B is processed using a similar but independent feature extraction path.

The resulting feature vectors from all three signal branches are concatenated and passed through a global attention block, which enables the model to prioritize information across the different inputs. The scalar thickness value h is then concatenated to this combined feature representation to condition the network's prediction on film thickness. The final layers consist of a series of fully connected layers that map the fused features to three outputs: the refractive indices n_x, n_y, and n_z.

The model comprises approximately 186,000 trainable parameters and is optimized using the Adam optimizer with a mean squared error loss function. For training, we generated a synthetic data set of 26 million samples using the `ReticoloFilmStack` package. Each sample corresponds to a unique combination of refractive indices within the range $n_i \in [1.3, 4.0]$ and thickness values $h \in [200, 800]$ nm. In all generated data sets, the substrate was assumed to be Si, consistent with the experimental samples studied. For measurements involving different substrate materials, new data sets must be generated to account for the modified optical response; however, the network architecture of the model remains unchanged. To align the training data with realistic experimental conditions, the preprocessing pipeline introduces additive Gaussian noise ($\sigma \in [0.001, 0.01]$), normalizes cross sections to (0,1), crops the central angular region affected by the vortex singularity, and resizes to reduce the sensitivity to local defects. These steps ensure that the network learns robust features representative of practical reflectance profiles, enabling generalization to experimental data. The idea of improving robustness via input perturbations is conceptually supported by stability training in deep neural networks.[46] By training the model only on three azimuthal slices instead of the full 2D far-field, we significantly reduce the dimensionality and computational load while preserving the directional sensitivity necessary to infer anisotropy.

RESULTS AND DISCUSSION

AnisoVision Model Performance. To evaluate the predictive accuracy and generalization capability of the AnisoVision model, we conducted both training-validation tracking and targeted performance testing on a held-out test set. The model was trained for 10 epochs using the synthetic data set described previously, with the learning progress monitored via the mean absolute error (MAE) metric on both training and validation sets. As shown in Figure 4(a), the

https://doi.org/10.1021/acsphotonics.5c02153
ACS Photonics 2026, 13, 224–235

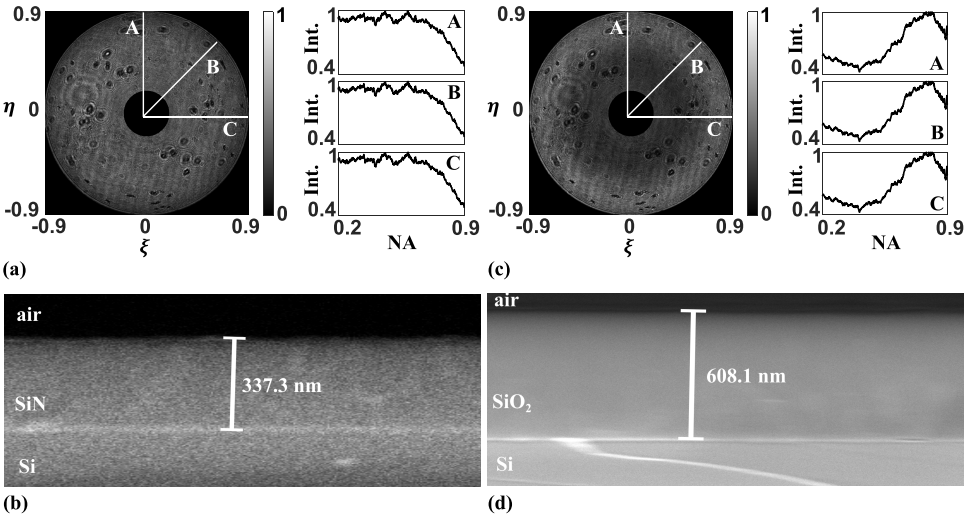

Figure 5. Experimental validation of the AnisoVision framework on isotropic films. (a) Measured far-field and normalized cross sections (A–C) for SiN on Si; (b) cross-sectional SEM image showing SiN thickness of 337.3 nm. (c) Measured far-field and normalized cross sections (A–C) for SiO_2 on Si; (d) SEM image showing SiO_2 thickness of 608.1 nm.

model exhibits stable convergence behavior, reaching a final validation MAE of 0.0758 after 10 epochs.

While the training data set was constructed from uniformly sampled combinations of film thickness $h \in [200, 800]$ nm (sampled in 10 nm steps) and refractive indices $n_i \in [1.3, 4.0]$ (sampled in steps of 0.02), we further evaluated the model's ability to interpolate and generalize to unseen combinations within these ranges. To this end, we generated a test set consisting of 10,000 random configurations, sampled across the same parameter space. The model's predictions on this randomized test set are shown in Figure 4(b–d), where true versus predicted values for n_x, n_y, and n_z are plotted, demonstrating the prediction density. The model demonstrates excellent agreement between true and predicted values across the entire refractive index range, with componentwise MAEs of 0.065 for n_x, 0.072 for n_y, and 0.085 for n_z. Among the three components, the model shows a slightly higher error for n_z. This reduced accuracy can be attributed to the inherently lower sensitivity of the far-field signal to the out-of-plane permittivity ε_z, particularly for thinner layers. The influence of n_z on the angular reflectance is comparatively weaker and highly dependent on layer thickness h, making its contribution more difficult to resolve.

To obtain a more statistically robust assessment of prediction error, we also computed the percentage error for each component across the 10,000 test samples and summarized the distributions as box plots in Figure 4(e). The median percentage error for in-plane indices n_x and n_y was 1.582 and 1.820%, respectively, while for n_z, it was 2.292%. These low percentage errors indicate that the model captures the underlying physics and anisotropic trends of the reflectivity process with high fidelity, even in unseen regions of the parameter space. Moreover, we observe that the MAE is worse at higher refractive indices (as can be seen in Figure 4(d)); however, such high refractive index values are uncommon outside narrow resonance bands.[47] Therefore, for most real materials with moderate and smoothly varying indices, where the model performs with a significantly lower error, the method is expected to perform even better than what is indicated in Figure 4(e). More details on the performance of the AnisoVision model are provided in Section 2 of the Supporting Information. Further, a quantitative evaluation of the error estimation in the retrieved optical constants from AnisoVision under experimentally relevant noise and thickness deviations is provided in Section 3 of the Supporting Information.

Optical Characterization of Isotropic Materials. To experimentally validate the accuracy and robustness of the proposed approach, we applied the AnisoVision model to characterize two well-known isotropic dielectric films: silicon nitride (SiN) and silicon dioxide (SiO_2). These materials serve as important reference samples to confirm that the framework can reliably extract refractive index values when the sample exhibits no in-plane and out-of-plane anisotropy, i.e., $n_x = n_y = n_z$.

Figure 5(a) shows the measured far-field reflectance pattern for the SiN sample (air/SiN/Si), captured at the back focal plane with the central region cropped due to the vortex-induced singularity. The three cross-sectional slices: A (ϕ = 0°), B (ϕ = 45°), and C (ϕ = 90°) are also shown as normalized intensity profiles. As expected for an isotropic film, the angular reflectance pattern is radially symmetric, and thus, the intensity variations along different azimuthal directions are nearly identical. This radial symmetry enables profile averaging, which improves the signal-to-noise ratio and reduces the impact of scattering artifacts caused by surface dust or imperfections across the objective's aperture. The corresponding cross-sectional SEM image of the SiN sample is shown in Figure 5(b). The SiN layer thickness is measured to be h = 337.3 nm. Details of the SEM preparation and imaging procedure are provided in Section 4 of the Supporting Information. Using this thickness as input to the AnisoVision model, we retrieved the refractive indices as $n_x = n_y = n_z$ = 2.057, which is in good agreement with the literature values for SiN at the wavelength of 633 nm.[48]

Similarly, Figure 5(c) shows the measured far-field pattern for the SiO_2 sample (air/SiO_2/Si), again exhibiting radial symmetry across the three angular slices. The corresponding SEM image in Figure 5(d) reveals a film thickness of h = 608.1 nm. Using this value in AnisoVision yields the retrieved refractive indices $n_x = n_y = n_z$ = 1.469, which also agrees well with standard reported values for SiO_2 at this wavelength.[49,50]

https://doi.org/10.1021/acsphotonics.5c02153
ACS Photonics 2026, 13, 224–235

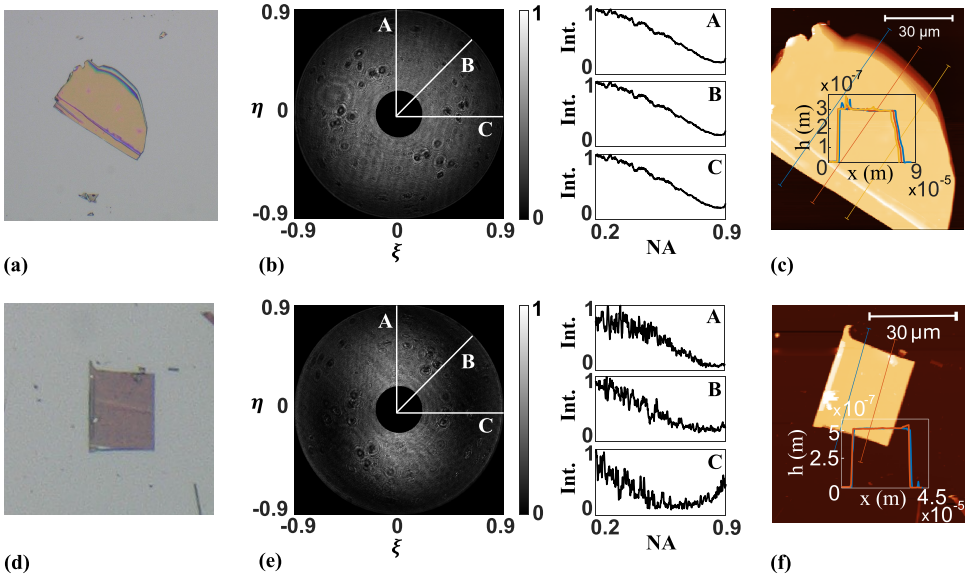

Figure 6. Optical characterization of anisotropic van der Waals materials using AnisoVision. (a) Optical microscope image of an exfoliated h-BN flake. (b) Measured far-field intensity profile (central region cropped) and normalized cross-sectional slices A (0°), B (45°), and C (90°) for h-BN, showing radial symmetry due to uniaxial anisotropy. (c) Atomic force microscopy (AFM) image of the h-BN flake, indicating a thickness of 300 nm. (d) Optical microscope image of an exfoliated α-MoO_3 flake. (e) Orientation-corrected far-field intensity profile and corresponding cross sections A−C, revealing asymmetry due to biaxial anisotropy. (f) AFM image of the α-MoO_3 flake, indicating a thickness of 510 nm.

These two examples demonstrate that the proposed deep learning-based CFS framework is capable of accurately retrieving isotropic refractive index values from the experimental far-field data. The radial polarization illumination, combined with the model's ability to focus on key angular features, ensures robustness to noise and spatial inhomogeneities in the optical system.

Optical Characterization of van der Waals Materials. To demonstrate the generalizability of our technique beyond conventional isotropic materials, we apply it to characterize thin exfoliated flakes of van der Waals (vdW) materials. In this section, we present results on two representative materials: hexagonal-BN (h-BN) and α-MoO_3, which exhibit uniaxial and biaxial optical anisotropy, respectively. These materials are widely studied in nanophotonics for their unique optical responses and anisotropic dielectric properties.[51,52] h-BN is a wide-bandgap (~6 eV) layered material composed of alternating boron and nitrogen atoms in a hexagonal lattice. It is optically transparent across a broad spectral range and exhibits pronounced uniaxial anisotropy due to its anisotropic crystal structure. The in-plane refractive index ($n_x = n_y$) and out-of-plane index (n_z) differ significantly, with reported anisotropy $\Delta n \approx 0.3-0.7$ in the visible range.[7,53] These properties make h-BN an ideal platform for nanoscale optical confinement, quantum emitters, and hyperbolic dispersion. α-MoO_3 is a strongly birefringent vdW crystal that exhibits a monoclinic lattice structure, resulting in three distinct principal refractive indices ($n_x \neq n_y \neq n_z$). This biaxial character leads to asymmetric light-matter interactions, enabling applications in mid-infrared photonics, in-plane hyperbolicity, and directionally dependent excitonic responses.[2,3,5,9] Mechanical exfoliation of α-MoO_3 yields optically flat flakes suitable for far-field optical studies. Due to the nature of mechanical exfoliation, the flakes used in this study exhibit variation in lateral dimensions, thickness, and in-plane crystal orientation. To correct for rotational misalignment of the far-field patterns, we apply a symmetry-based algorithm (see Appendix Rotation of Far-field Images) to infer the principal crystal axes and align the far-field data accordingly.

Figure 6(a) shows an optical microscope image of the h-BN flake characterized in this study. The corresponding measured far-field pattern (after cropping the central vortex region) is shown in Figure 6(b), along with the normalized cross-sectional profiles A−C at azimuthal angles 0, 45, and 90°, respectively. As expected for a uniaxial crystal with no in-plane anisotropy, the far-field exhibits radial symmetry, allowing us to average the profiles across all azimuthal directions to suppress experimental noise. The height of the flake was measured using atomic force microscopy (AFM), as shown in Figure 6(c), yielding a thickness of h = 300 nm (details of the AFM measurements are provided in Section 5 of the Supporting Information). Using this value as input to the AnisoVision model, we retrieve the refractive indices $n_x = n_y = 2.109$ and $n_z = 1.485$, which correspond to an out-of-plane anisotropy $\Delta n_{xz} = \Delta n_{yz} = 0.624$. These results are in agreement with previously reported values at 633 nm, including $n_x = n_y = 2.126$ and $n_z = 1.567$ from Zotev et al.,[1] $n_x = n_y = 2.215$ and $n_z = 1.601$ from Grudinin et al.,[7] and $n_x = n_y = 2.137$ and $n_z = 1.851$ from Rah et al.[54]

Figure 6(d) shows an optical microscope image of an exfoliated α-MoO_3 flake. The far-field, corrected for orientation, is shown in Figure 6(e), along with the extracted normalized cross-sectional profiles A, B, and C. Unlike h-BN, the far-field distribution of α-MoO_3 is clearly anisotropic, confirming the presence of strong in-plane anisotropy. To reduce noise while preserving directional information, we average the profiles only over azimuthally equivalent directions: A over 0 and 180°, B over 45, 135, 225, and 315°, and C over 90 and 270°. The flake height was measured via AFM (Figure 6(f)) to be h = 510 nm. Using AnisoVision, we retrieve $n_x = 2.297$, $n_y = 2.229$, and $n_z = 1.926$, leading to in-plane anisotropic value of $\Delta n_{xy} = 0.068$, and out-of-plane anisotropic values of $\Delta n_{xz} = 0.371$, and $\Delta n_{yz} = 0.303$. These results are in agreement with previously reported anisotropic

https://doi.org/10.1021/acsphotonics.5c02153
ACS Photonics 2026, 13, 224−235

indices at 633 nm, n_x = 2.230, n_y = 2.220, and n_z = 1.969 by Andres-Penares et al.[12]

These experiments validate the ability of our framework to accurately extract full dielectric tensor components from far-field intensity profiles of anisotropic 2D materials without requiring prior knowledge of the crystal orientation or using polarization-resolved detection.

AnisoVision Model Stability with Varying Heights. To further validate the robustness of AnisoVision, we assess its stability in retrieving consistent optical properties across samples of the same material, but with varying thicknesses. While the height of an anisotropic film significantly influences the resulting far-field patterns, the underlying refractive indices of the material remain constant. Therefore, an accurate and reliable model should consistently recover the same n_x, n_y, n_z values irrespective of layer thickness.

To test this, we study 12 different mechanically exfoliated flakes of α-MoO_3, each with a distinct thickness due to the random nature of exfoliation. These flakes exhibit various lateral dimensions and thicknesses ranging from approximately 380 to 720 nm. The far-field angular distributions of all 12 samples are shown in Section 6 of the Supporting Information. The corresponding flake thicknesses were precisely determined by using AFM, and the measured heights were used as inputs to AnisoVision for retrieval. In Table 1, we summarize the retrieved values of n_x, n_y, and n_z along with the corresponding heights h for each of the 12 flakes. In Figure 7(a–c), we present the predicted values of n_x, n_y, and n_z as a function of layer thickness h, respectively. Despite significant variation in height across the samples, the retrieved refractive indices remain consistent (more analysis is provided in Section 7 of the Supporting Information). Specifically, the mean retrieved values are n_x = 2.291, n_y = 2.207, and n_z = 1.947, with standard deviations of 0.0274, 0.0307, and 0.0303, respectively. These results not only fall within the expected experimental uncertainty but also agree well with literature-reported values for α-MoO_3.[12]

Table 1. Retrieved Refractive Indices n_x, n_y, and n_z for 12 Exfoliated α-MoO_3 Flakes of Varying Thicknesses

Flake	h (nm)	n_x	n_y	n_z
1	383	2.3472	2.2882	1.9197
2	475	2.3894	2.2338	2.0720
3	495	2.2340	2.0806	1.8520
4	503	2.2728	2.2317	2.0087
5	510	2.2975	2.2299	1.9264
6	511	2.2496	2.2308	1.9283
7	538	2.2466	2.1534	1.9371
8	608	2.2703	2.2078	1.9282
9	608	2.2709	2.1727	1.9385
10	608	2.2357	2.1678	1.9237
11	721	2.2961	2.2546	2.0103
12	735	2.3776	2.2283	1.9229

The slight fluctuations observed are attributed primarily to sample imperfections, surface roughness, and minor experimental noise rather than model instability. The low spread in retrieved indices demonstrates the stability and reliability of AnisoVision when applied to realistic, variable-thickness flakes, further reinforcing its utility for the high-throughput characterization of 2D anisotropic materials.

Joint Retrieval of Thickness and Refractive Index Using Cross-Flake Consistency. When multiple flakes of the same material with different thicknesses are available, the height-refractive index ambiguity can be resolved without explicitly using height as an input. While the AnisoVision model typically requires the flake thickness as an input to resolve the inherent coupling between the optical path length and refractive index, this dependency can be bypassed when multiple flakes of the same material but different thicknesses are available. In such cases, the model is evaluated for each flake across a range of candidate thicknesses. The correct thickness values are those that yield consistent refractive index predictions across all of the flakes. Because only the true thicknesses produce a common triplet (n_x, n_y, n_z) for all flakes, this method enables simultaneous retrieval of both thickness and refractive indices purely from the consistency constraint across samples.

When several flakes belong to the same anisotropic material, they share the same intrinsic refractive indices but have different thicknesses h_i. For each flake i, the trained model predicts $n_i^{\mathrm{pred}}(h) = (n_{x,i}(h), n_{y,i}(h), n_{z,i}(h))$ when evaluated at a candidate height h. If the assumed height is incorrect, the prediction compensates for the wrong optical path length and therefore deviates from the true material refractive index, and only the correct thicknesses will produce refractive index

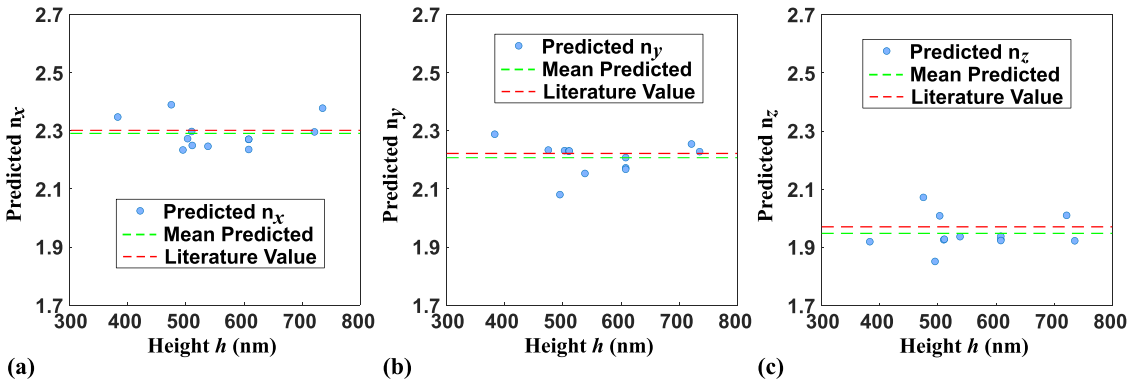

Figure 7. Stability test of AnisoVision for α-MoO_3 flakes of varying thicknesses. Each point corresponds to a retrieved refractive index (n_x in panel (a), n_y in panel (b), or n_z in panel (c)) for a single flake, plotted as a function of the measured height. The red dashed line indicates the expected (literature) value, while the green dotted line shows the mean of the predicted values. Despite changes in thickness, the model consistently predicts the same optical properties.

https://doi.org/10.1021/acsphotonics.5c02153
ACS Photonics 2026, 13, 224–235

predictions that agree across all flakes: $n_1^{\text{pred}}(h_1) \approx n_2^{\text{pred}}(h_2) \approx \cdots \approx n$.

For each flake i, we evaluate the model over a discrete height range $h_i \in [h^{\min}, h^{\max}]$, storing $n_i^{\text{pred}}(h_i)$. For any combination of heights $h_1, \cdots, h_F$ across flakes, we compute the maximum interflake deviation: $\Delta(h_i, \cdots, h_F) = \max_i n_i^{\text{pred}}(h_i) - \min_i n_i^{\text{pred}}(h_i)$. A combination is accepted if $\|\Delta(h_1, \ldots, h_F)\|_\infty < \varepsilon$, meaning the predicted indices agree within a small tolerance ε. All accepted height combinations form the "consistent solution set," from which we compute the refined thickness for each flake (mean ± std of all accepted h_i). This is a robust method because the far-field reflectance depends on the optical path length. If an incorrect height is provided, the network's predicted refractive index shifts to compensate. Therefore, flakes of the same material will only produce consistent refractive index predictions when their correct heights are used. This removes the intrinsic n-h coupling without requiring height as an explicit input or as a trainable output, as shown in Table 2. However, the accuracy and std deviation are higher than we can achieve if the NN model is used to do the same.

Table 2. Recovered Thicknesses and Predicted Refractive Indices for Two α-MoO_3 Flakes Using Cross-Flake Consistency

h^{AFM} (nm)	$h^{\text{retrieved}}$ (nm)	$\Delta h^{\text{retrieved}}$ (nm)	n_x	n_y	n_z
510	515	16	2.3026	2.1453	1.9791
735	715	21	2.3145	2.1620	1.9953

While this cross-flake approach allows estimation of both thickness and refractive indices using only far-field reflectance data, it requires data of two or more flakes of the same material. For single flakes, AnisoVision still provides accurate single-shot predictions of refractive indices, but the height must be measured independently, e.g., by using AFM/SEM.

CONCLUSIONS

In conclusion, we developed AnisoVision, a neural network-based framework for retrieving the full anisotropic refractive index tensor (n_x, n_y, n_z) from single-shot far-field reflectance measurements acquired using CFS under tightly focused radially polarized illumination. The model was validated using both simulations and experiments across isotropic (SiN and SiO_2), uniaxial (h-BN), and biaxial (α-MoO_3) materials. We achieved mean absolute errors of 0.065, 0.072, and 0.085 for n_x, n_y, and n_z, respectively, and experimentally predicted refractive indices were in agreement with previously reported literature values. Compared with ellipsometry-based approaches, our method enables single-shot, localized, and inline measurement of the full anisotropic refractive index tensor using far-field reflectance under tightly focused illumination. It does not require sample rotation, grazing-incidence setups, or spatial averaging. As a result, it is inherently compatible with nanoscale flakes and layered materials with high anisotropy. Further, while analytical fitting is feasible for simple three-interface systems under specific polarization conditions, the problem becomes significantly more complex for anisotropic flakes with arbitrary orientations, variable thicknesses, and multidimensional far-field reflectance responses. In such cases, the reflectance profile is a high-dimensional function of n_x, n_y, n_z, and h, and traditional analytical models either become cumbersome or require simplifying assumptions that reduce generality. The deep learning approach allows the model to learn full nonlinear mapping from cross-sectional reflectance data and thickness to the refractive indices, automatically capturing subtle correlations and material anisotropies. This provides a generalizable and computationally efficient tool for predicting refractive indices across a wide range of materials and geometries, including cases where explicit analytical solutions are difficult to derive or are impractically complex. Furthermore, even though the model uses height as an input to ensure identifiability, we show that when multiple flakes of the same material are available, the joint estimation of both thickness and refractive indices can be performed using a cross-flake consistency criterion without requiring height input. This further enhances the self-sufficiency and applicability of the method. Finally, while this study focused on monochromatic operation at λ = 633 nm, the method is readily extensible to multispectral or broadband implementations. In particular, two-pulse broadband CFS, as demonstrated by van der Sijs et al.,[55] could enable single-shot, spectrally resolved anisotropic characterization, paving the way toward dispersion-sensitive metrology using the same framework.

APPENDIX

Sample Preparation

SiN/SiO_2 on Si. The samples consist of a thin layer of SiN or SiO_2 on a Si substrate. The samples are fabricated on a standard 525 μm thick Si wafer. The wafer is first cleaved into 15 mm × 15 mm samples, and cleaned in acetone and isopropanol (IPA) using an ultrasonic bath. Subsequently, we deposited a 337.3 nm silicon nitride and a 608.1 nm silicon dioxide layer, respectively, on the substrates via inductively coupled plasma chemical vapor deposition (ICPCVD, Oxford PlasmaPro100). ICPCVD is known for enhanced deposition uniformity and minimized edge effects, which are beneficial for accurate refractive index determination. The depositions are carried out at a table temperature of 150 °C and a chamber pressure of 8 mTorr.

h-BN on Si. The sample consists of flakes of h-BN on a Si substrate. The Si substrate was first acid-cleaned, followed by organic cleaning with acetone, IPA, and DI water in an ultrasonic bath. The h-BN flake was fabricated by mechanically exfoliating commercially available bulk h-BN (HQ Graphene) using the scotch tape method. The flakes were thinned down by a few exfoliations on the tape itself and then exfoliated on the Si substrate.

α-MoO_3 on Si. The sample consists of flakes of α-MoO_3 on a Si substrate. Bulk α-MoO_3 crystals were acquired from 2D Semiconductors. The flakes were mechanically exfoliated from the bulk crystals and transferred onto the Si substrates (350 μm in thickness) using a poly(dimethylsiloxane) (PDMS)-based exfoliation and transfer method (X0 retention, DGL type, Gelpak) at 90 °C.

Rotation of Far-Field Images

In this section, we outline the method used to correct for the unknown crystal axis orientation in mechanically exfoliated biaxial flakes. For such flakes, the in-plane crystal axes can be randomly rotated with respect to the laboratory reference frame. To accurately retrieve the anisotropic refractive indices n_x, n_y, n_z, the measured far-field must first be realigned such that the in-plane optical axes align with fixed angular directions (e.g., ϕ = 0, 45, 90°) used by the AnisoVision model. As illustrated in Figure 8(a), we begin with the measured far-field

https://doi.org/10.1021/acsphotonics.5c02153
ACS Photonics 2026, 13, 224−235

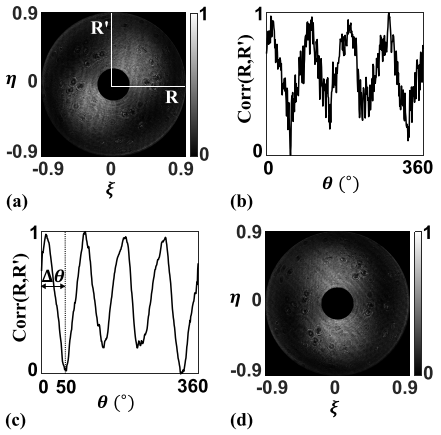

Figure 8. (a) Measured far-field pattern from an exfoliated α-MoO_3 flake, with two orthogonal radial profiles R and R' shown. (b) Computed correlation function corr2(R,R') between radial pairs as a function of rotation angle. (c) Smoothed correlation function showing the reduced correlation at $\Delta\theta$ = 50°. (d) Far-field image after rotational correction by $\Delta\theta$, aligned with the crystal axes.

pattern for an exfoliated α-MoO_3 flake. Two orthogonal radial line profiles, R and R', are extracted at angles separated by 90°. In general, if the crystal axes are not aligned with these radial directions, the two profiles will be correlated due to mixed index contributions. However, when the crystal axes align with R and R', the optical response becomes independent of the orthogonal in-plane index, minimizing the correlation between the two profiles.

To systematically identify this alignment, we define an angular correlation function:

$$\mathrm{corr2}(R, R') = \frac{\sum_{i=1}^{N}(R_\theta - \bar{R}_\theta)(R'_\theta - \bar{R}'_\theta)}{\sqrt{(\sum_{i=1}^{N}(R_\theta - \bar{R}_\theta)^2)(\sum_{i=1}^{N}(R'_\theta - \bar{R}'_\theta)^2)}} \quad (4)$$

where R_θ and R'_θ denote radial intensity profiles extracted from directions θ and θ + 90°, respectively, and $\bar{R}_\theta$ and $\bar{R}'_\theta$ are the means of the respective profiles.

By evaluating corr2(R,R') over the full 0° to 360° range, as shown in Figure 8(b), we observe a periodic function with fourfold symmetry, as expected due to the equivalence of quadrants in the far-field. To improve robustness and suppress high-frequency noise, we apply a smoothing filter to the correlation function, as shown in Figure 8(c) (both Figure 8(b,c) are normalized between 0 and 1 for consistency and clarity in comparison). The global minimum in the smoothed curve indicates the angular offset $\Delta\theta$ needed to align the crystal axes with the reference coordinate system used in AnisoVision. For the case shown, we find $\Delta\theta$ = 50°. After rotating the original far-field image by $\Delta\theta$, we obtain the corrected field shown in Figure 8(d). This aligned far-field is then used to extract the azimuthal cross sections A, B, and C at 0, 45, and 90°, respectively, and fed into the AnisoVision model for the optical characterization of the material. This procedure ensures consistent and physically meaningful extraction of the anisotropic optical parameters from arbitrarily oriented exfoliated flakes.

■ ASSOCIATED CONTENT

Supporting Information

The Supporting Information is available free of charge at https://pubs.acs.org/doi/10.1021/acsphotonics.5c02153.

Microscope objective calibration, AnisoVision performance, Error estimation in retrieved optical constants from experimental data, cross-sectional SEM details, AFM measurement details, far-field images and AFM profiles of α-MoO_3 flakes of different heights, and AnisoVision stability with varying heights (PDF)

■ AUTHOR INFORMATION

Corresponding Author

Anubhav Paul − *Imaging Physics Department, Faculty of Applied Sciences, Delft University of Technology, 2628 CJ Delft, The Netherlands;* orcid.org/0000-0002-4167-6256; Email: A.Paul-1@tudelft.nl

Authors

Kumar Rishav − *Imaging Physics Department, Faculty of Applied Sciences, Delft University of Technology, 2628 CJ Delft, The Netherlands;* orcid.org/0000-0002-4050-2238

Guus Klootwijk − *Imaging Physics Department, Faculty of Applied Sciences, Delft University of Technology, 2628 CJ Delft, The Netherlands*

Mitradeep Sarkar − *ICFO-Institut de Ciencies Fotoniques, The Barcelona Institute of Science and Technology, 08860 Castelldefels (Barcelona), Spain;* orcid.org/0000-0002-3431-0678

Onima Bisht − *Department of Quantum Nanoscience, Faculty of Applied Sciences, Delft University of Technology, 2628 CJ Delft, The Netherlands*

Zizheng Li − *Imaging Physics Department, Faculty of Applied Sciences, Delft University of Technology, 2628 CJ Delft, The Netherlands;* orcid.org/0000-0001-8139-8660

Sonia Conesa-Boj − *Department of Quantum Nanoscience, Faculty of Applied Sciences, Delft University of Technology, 2628 CJ Delft, The Netherlands*

Georgia T. Papadakis − *ICFO-Institut de Ciencies Fotoniques, The Barcelona Institute of Science and Technology, 08860 Castelldefels (Barcelona), Spain*

Silvania F. Pereira − *Imaging Physics Department, Faculty of Applied Sciences, Delft University of Technology, 2628 CJ Delft, The Netherlands*

Complete contact information is available at: https://pubs.acs.org/10.1021/acsphotonics.5c02153

Funding

A.P. and S.F.P. acknowledge the Nederlandse Organisatie voor Wetenschappelijk Onderzoek (Project 17−24 Synoptics No. 2) for funding this research. M.S. and G.T.P. acknowledge Caixa Foundation (ID 100010434), the Spanish MICINN (PID2021−125441OA-I00, PID2020−112625GB-I00, and CEX2019−000910-S), the European Union (CATHERINA, 101168064 and LCF/BQ/PI21/11830019 under the Marie Skłodowska-Curie Grant Agreement No. 847648), Generalitat de Catalunya (2021 SGR 01443), Fundació Cellex, and Fundació Mir-Puig.

Notes

The authors declare no competing financial interest.

https://doi.org/10.1021/acsphotonics.5c02153
ACS Photonics 2026, 13, 224−235

■ ACKNOWLEDGMENTS

The authors thank Tom Duivenvoorde of TNO for the AFM measurements. S.F.P. acknowledges the Institute of Photonics (ICFO) for its hospitality during her sabbatical. A.P. and S.F.P. acknowledge Dmytro Kolenov for his valuable involvement in the conceptualization of this work.

■ REFERENCES

(1) Zotev, P. G.; Wang, Y.; Andres-Penares, D.; Severs-Millard, T.; Randerson, S.; Hu, X.; Sortino, L.; Louca, C.; Brotons-Gisbert, M.; Huq, T.; et al. Van der Waals materials for applications in nanophotonics. *Laser Photonics Rev.* **2023**, *17*, No. 2200957.

(2) Dereshgi, S. A.; Lee, Y.-S.; Larciprete, M. C.; Centini, M.; Dravid, V. P.; Aydin, K. Low-Symmetry α-MoO3 Heterostructures for Wave Plate Applications in Visible Frequencies. Advanced. *Opt. Mater.* **2023**, *11*, No. 2202603.

(3) Álvarez-Pérez, G.; Folland, T. G.; Errea, I.; Taboada-Gutiérrez, J.; Duan, J.; Martín-Sánchez, J.; Tresguerres-Mata, A. I.; Matson, J. R.; Bylinkin, A.; He, M.; et al. Infrared permittivity of the biaxial van der waals semiconductor α-MoO3 from near-and far-field correlative studies. *Adv. Mater.* **2020**, *32*, No. 1908176.

(4) Lu, B.; Xia, Y.; Ren, Y.; Xie, M.; Zhou, L.; Vinai, G.; Morton, S. A.; Wee, A. T.; van der Wiel, W. G.; Zhang, W.; Wong, P. K. J. When machine learning meets 2D materials: a review. *Adv. Sci.* **2024**, *11*, No. 2305277.

(5) Enders, M. T.; Sarkar, M.; Giteau, M.; Deeva, A.; Herzig Sheinfux, H.; Shokooh-Saremi, M.; Koppens, F. H.; Papadakis, G. T. Deeply subwavelength mid-infrared phase retardation with α-MoO3 flakes. *Commun. Mater.* **2024**, *5*, No. 16.

(6) Sarkar, M.; Giteau, M.; Enders, M. T.; Papadakis, G. T. Lithography-free directional control of thermal emission. *Nanophotonics* **2024**, *13*, 763−771.

(7) Grudinin, D. V.; Ermolaev, G.; Baranov, D.; Toksumakov, A.; Voronin, K.; Slavich, A.; Vyshnevyy, A.; Mazitov, A.; Kruglov, I.; Ghazaryan, D.; et al. Hexagonal boron nitride nanophotonics: a record-breaking material for the ultraviolet and visible spectral ranges. *Mater. Horiz.* **2023**, *10*, 2427−2435.

(8) Shen, W.; Yu, Y.; Huang, Y.; Ma, G.; Yao, C.; Sun, L.; Hu, C. Origins and cavity-based regulation of optical anisotropy of α-MoO3 crystal. *2D Mater.* **2023**, *10*, No. 015024.

(9) Lajaunie, L.; Boucher, F.; Dessapt, R.; Moreau, P. Strong anisotropic influence of local-field effects on the dielectric response of α-MoO 3. *Condens.-Matter Mater. Phys.* **2013**, *88*, No. 115141.

(10) Erman, M.; Theeten, J. Spatially resolved ellipsometry. *J. Appl. Phys.* **1986**, *60*, 859−873.

(11) Ma, Y.; Lu, S.; Dong, X.; Han, G.; Chen, Z.; Liu, Y. Optical parameters of graphene/MoS2 van der Waals heterostructure investigated by spectroscopic ellipsometry. *Appl. Surf. Sci.* **2022**, *599*, No. 153987.

(12) Andres-Penares, D.; Brotons-Gisbert, M.; Bonato, C.; Sánchez-Royo, J. F.; Gerardot, B. D. Optical and dielectric properties of MoO3 nanosheets for van der Waals heterostructures. *Appl. Phys. Lett.* **2021**, *119*, No. 223104.

(13) Slavich, A. S.; Ermolaev, G. A.; Tatmyshevskiy, M. K.; Toksumakov, A. N.; Matveeva, O. G.; Grudinin, D. V.; Voronin, K. V.; Mazitov, A.; Kravtsov, K. V.; Syuy, A. V.; et al. Exploring van der Waals materials with high anisotropy: geometrical and optical approaches. *Light:Sci. Appl.* **2024**, *13*, No. 68.

(14) Ermolaev, G. A.; Voronin, K. V.; Toksumakov, A. N.; Grudinin, D. V.; Fradkin, I. M.; Mazitov, A.; Slavich, A. S.; Tatmyshevskiy, M. K.; Yakubovsky, D. I.; Solovey, V. R.; et al. Wandering principal optical axes in van der Waals triclinic materials. *Nat. Commun.* **2024**, *15*, No. 1552.

(15) Chen, C.; Chen, X.; Wang, C.; Sheng, S.; Song, L.; Gu, H.; Liu, S.; Imaging, M. ueller matrix ellipsometry with sub-micron resolution based on back focal plane scanning. *Opt. Express* **2021**, *29*, 32712−32727.

(16) Kenaz, R.; Ghosh, S.; Ramachandran, P.; Watanabe, K.; Taniguchi, T.; Steinberg, H.; Rapaport, R. Thickness mapping and layer number identification of exfoliated van der Waals materials by Fourier imaging micro-ellipsometry. *ACS Nano* **2023**, *17*, 9188−9196.

(17) Yang, D.-G.; Ghim, Y.-S.; Rhee, H.-G. High precision micro-ellipsometry based on a pixelated polarizing camera. *Optics Lasers Eng.* **2024**, *178*, No. 108240.

(18) He, M.; Folland, T. G.; Duan, J.; Alonso-González, P.; De Liberato, S.; Paarmann, A.; Caldwell, J. D. Anisotropy and Modal Hybridization in Infrared Nanophotonics Using Low-Symmetry Materials. *ACS Photonics* **2022**, *9*, 1078−1095.

(19) Politano, G. G.; Versace, C. Spectroscopic ellipsometry: advancements, applications and future prospects in optical characterization. *Spectrosc. J.* **2023**, *1*, 163−181.

(20) Shen, W.; Hu, C.; Tao, J.; Liu, J.; Fan, S.; Wei, Y.; An, C.; Chen, J.; Wu, S.; Li, Y.; et al. Resolving the optical anisotropy of low-symmetry 2D materials. *Nanoscale* **2018**, *10*, 8329−8337.

(21) Nørgaard, M.; Yezekyan, T.; Rolfs, S.; Frydendahl, C.; Mortensen, N. A.; Zenin, V. A. Near-field refractometry of van der Waals crystals. *Nanophotonics* **2025**, *14*, 2473−2483.

(22) Guo, X.; Bertling, K.; Rakić, A. D. Optical constants from scattering-type scanning near-field optical microscope. *Appl. Phys. Lett.* **2021**, *118*, No. 041103.

(23) Siebenkotten, D.; Kästner, B.; Marschall, M.; Hoehl, A.; Amakawa, S. Calibration method for complex permittivity measurements using s-SNOM combining multiple probe tapping harmonics. *Opt. Express* **2024**, *32*, 23882−23893.

(24) Khadir, S.; Bon, P.; Vignaud, D.; Galopin, E.; McEvoy, N.; McCloskey, D.; Monneret, S.; Baffou, G. Optical imaging and characterization of graphene and other 2D materials using quantitative phase microscopy. *ACS Photonics* **2017**, *4*, 3130−3139.

(25) Paul, A.; Rafighdoost, J.; Dou, X.; Pereira, S. F. Investigation of coherent Fourier scatterometry as a calibration tool for determination of steep side wall angle and height of a nanostructure. *Meas. Sci. Technol.* **2024**, *35*, No. 075202.

(26) Kumar, N.; Petrik, P.; Ramanandan, G. K.; El Gawhary, O.; Roy, S.; Pereira, S. F.; Coene, W. M. J. M.; Urbach, H. P. Reconstruction of sub-wavelength features and nano-positioning of gratings using coherent Fourier scatterometry. *Opt. Express* **2014**, *22*, 24678−24688.

(27) Paul, A.; Kolenov, D.; Scholte, T.; Pereira, S. F. Coherent Fourier scatterometry: a holistic tool for inspection of isolated particles or defects on gratings. *Appl. Opt.* **2023**, *62*, 7589−7595.

(28) López-Morales, G.; Rico-Botero, V.-M.; Espinosa-Luna, R.; Zhan, Q. Refractive index measurement of dielectric samples using highly focused radially polarized light. *Chin. Opt. Lett.* **2017**, *15*, No. 030004.

(29) Paul, A.; Wever, R.; Soman, S.; Pereira, S. F. Utilizing focused field as a probe for shape determination of subwavelength structures via coherent Fourier scatterometry. *Phys. Rev. Appl.* **2025**, *23*, No. 024016.

(30) Zuo, C.; Qian, J.; Feng, S.; Yin, W.; Li, Y.; Fan, P.; Han, J.; Qian, K.; Chen, Q. Deep learning in optical metrology: a review. *Light:Sci. Appl.* **2022**, *11*, No. 39.

(31) Zhang, L.; Shao, S. Image-based machine learning for materials science. *J. Appl. Phys.* **2022**, *132*, No. 100701.

(32) Li, Y.; Wu, Y.; Yu, H.; Takeuchi, I.; Jaramillo, R. Deep learning for rapid analysis of spectroscopic ellipsometry data. *Adv. Photonics Res.* **2021**, *2*, No. 2100147.

(33) Mao, Y.; Wang, L.; Chen, C.; Yang, Z.; Wang, J. Thickness determination of ultrathin 2D materials empowered by machine learning algorithms. *Laser Photonics Rev.* **2023**, *17*, No. 2200357.

(34) Xu, Y.; Xu, D.; Yu, N.; Liang, B.; Yang, Z.; Asif, M. S.; Yan, R.; Liu, M. Machine learning enhanced optical microscopy for the rapid morphology characterization of silver nanoparticles. *ACS Appl. Mater. Interfaces* **2023**, *15*, 18244−18251.

(35) Han, B.; Lin, Y.; Yang, Y.; Mao, N.; Li, W.; Wang, H.; Yasuda, K.; Wang, X.; Fatemi, V.; Zhou, L.; et al. Deep-learning-enabled fast

optical identification and characterization of 2D materials. *Adv. Mater.* **2020**, *32*, No. 2000953.
(36) Cao, Z.; Chen, Y.; Xian, F.; Ren, H.; Tu, B. Thin film characterization by learning-assisted multi-angle polarized microscopy. *Opt. Lett.* **2024**, *49*, 598−601.
(37) Liu, S.; Chen, X.; Yang, T.; Zhang, J.; Liu, S. Inverse optical scatterometry using sketch-guided deep learning. *Opt. Express* **2024**, *32*, 20303−20315.
(38) Kolenov, D.; Pereira, S. F. Machine learning techniques applied for the detection of nanoparticles on surfaces using coherent Fourier scatterometry. *Opt. Express* **2020**, *28*, 19163−19186.
(39) Ning, K.; Lu, B.; Wang, X.; Zhang, X.; Nie, S.; Jiang, T.; Li, A.; Fan, G.; Wang, X.; Luo, Q.; et al. Deep self-learning enables fast, high-fidelity isotropic resolution restoration for volumetric fluorescence microscopy. *Light:Sci. Appl.* **2023**, *12*, No. 204.
(40) Quabis, S.; Dorn, R.; Eberler, M.; Glöckl, O.; Leuchs, G. Focusing light to a tighter spot. *Opt. Commun.* **2000**, *179*, 1−7.
(41) Stratton, J. A. *Electromagnetic theory*; John Wiley & Sons, 2007.
(42) Berreman, D. W. Optics in stratified and anisotropic media: 4× 4-matrix formulation. *J. Opt. Soc. Am.* **1972**, *62*, 502−510.
(43) Bay, M. M.; Vignolini, S.; Vynck, K. PyLlama: A stable and versatile Python toolkit for the electromagnetic modelling of multilayered anisotropic media. *Comput. Phys. Commun.* **2022**, *273*, No. 108256.
(44) Hugonin, J.-P.; Lalanne, P. Analysis of stacks of anisotropic uniform layers: user guide for the RETICOLOfilm-stack program 2022 https://hal.science/hal-03899689.
(45) Porfirev, A. P.; Ustinov, A. V.; Khonina, S. N. Polarization conversion when focusing cylindrically polarized vortex beams. *Sci. Rep.* **2016**, *6*, No. 6.
(46) Laermann, J.; Samek, W.; Strodthoff, N. *Achieving Generalizable Robustness of Deep Neural Networks by Stability Training*; Pattern Recognition: Cham, 2019; pp 360−373.
(47) Shim, H.; Monticone, F.; Miller, O. D. Fundamental limits to the refractive index of transparent optical materials. *Adv. Mater.* **2021**, *33*, No. 2103946.
(48) Luke, K.; Okawachi, Y.; Lamont, M. R.; Gaeta, A. L.; Lipson, M. Broadband mid-infrared frequency comb generation in a Si3N4 microresonator. *Opt. Lett.* **2015**, *40*, 4823−4826.
(49) Rodríguez-de Marcos, L. V.; Larruquert, J. I.; Méndez, J. A.; Aznárez, J. A. Self-consistent optical constants of SiO2 and Ta2O5 films. *Opt. Mater. Express* **2016**, *6*, 3622−3637.
(50) Franta, D.; Nečas, D.; Ohlídal, I.; Giglia, A. In *Optical characterization of SiO2 thin films using universal dispersion model over wide spectral range*, Optical Micro-and Nanometrology VI; SPIE, 2016; pp 253−267.
(51) Lin, H.; Zhang, Z.; Zhang, H.; Lin, K.-T.; Wen, X.; Liang, Y.; Fu, Y.; Lau, A. K. T.; Ma, T.; Qiu, C.-W.; Jia, B. Engineering van der Waals Materials for Advanced Metaphotonics. *Chem. Rev.* **2022**, *122*, 15204−15355.
(52) Ajayan, P.; Kim, P.; Banerjee, K. Two-dimensional van der Waals materials. *Phys. Today* **2016**, *69*, 38−44.
(53) Segura, A.; Artús, L.; Cuscó, R.; Taniguchi, T.; Cassabois, G.; Gil, B. Natural optical anisotropy of h-BN: Highest giant birefringence in a bulk crystal through the mid-infrared to ultraviolet range. *Phys. Rev. Mater.* **2018**, *2*, No. 024001.
(54) Rah, Y.; Jin, Y.; Kim, S.; Yu, K. Optical analysis of the refractive index and birefringence of hexagonal boron nitride from the visible to near-infrared. *Opt. Lett.* **2019**, *44*, 3797−3800.
(55) van der Sijs, T. A.; Rafighdoost, J.; Siaudinyte, L.; Urbach, H. P.; Pereira, S. F.; El Gawhary, O. Broadband coherent Fourier scatterometry: A two-pulse approach. *Rev. Sci. Instrum.* **2025**, *96*, No. 013702.

https://doi.org/10.1021/acsphotonics.5c02153
ACS Photonics 2026, 13, 224−235